J. Fluid Mech. (2006), *vol.* 569, *pp.* 331–348.
doi:10.1017/S0022112006003077 Printed in the United Kingdom

Travelling circular waves in axisymmetric rotating convection

By J. M. LOPEZ[1], A. RUBIO[1] AND F. MARQUES[2]

[1]Department of Mathematics and Statistics, Arizona State University, Tempe AZ 85287, USA
[2]Departament de Física Aplicada, Univ. Politècnica de Catalunya, Barcelona 08034, Spain

(Received 22 March 2006 and in revised form 8 June 2006)

Rayleigh–Bénard convection in a finite rotating cylinder of moderate aspect ratio (radius four times the depth) is investigated numerically for a fluid of Prandtl number equal to 7 (corresponding essentially to water). We consider the effects of rotation from both the Coriolis force and the centrifugal force and find that the centrifugal force plays a significant dynamic role. In this initial study, we restrict the computations to the axisymmetric subspace in which the convection patterns near onset consist of steady concentric circular cells, the so-called target patterns, which have been studied and observed experimentally under different conditions by a number of investigators. As the convection is driven far enough beyond onset, the steady cellular patterns give way to time-periodic states in which the target patterns travel radially inward. We have identified two such travelling modes, primarily distinguished by one having alternating warm and cold plumes forming at the cylinder sidewall and then propagating radially inward to quench alternately cold and warm plumes on the axis. The other mode always has a cold plume descending on the sidewall and the adjacent warm plume periodically splits into two, with the innermost of the split pair travelling radially inward. The first of these modes is found when the centrifugal force is weak and the second for stronger centrifugal force. The large-scale meridional circulation driven by the centrifugal buoyancy is seen to favour having a cold plume descending on the sidewall, accounting for the switch to the second travelling mode.

1. Introduction

Rotating thermal convection is a paradigm problem that incorporates fundamental processes of great importance to atmospheric and oceanic circulations, as well as being of astrophysical importance. Early theoretical work considered an infinite layer of fluid between two plates maintained at constant temperatures (Veronis 1959; Chandrasekhar 1961). If the temperature difference is not too great, then the Boussinesq approximation can be implemented which treats fluid properties (viscosity, thermal diffusivity, and coefficient of volume expansion) as constants, assumes that density varies linearly with temperature and that density variations need only be taken into account in the buoyancy terms.

Traditionally, density variation was only incorporated in the gravitational buoyancy term and not in the centrifugal buoyancy term. This is valid only in the limit of vanishingly small centrifugal force relative to gravity. In this limit, the governing equations admit a trivial conduction solution, where the velocity corresponds to solid body rotation (which is a static state in the rotating frame) together with a linear temperature profile across the layer. A number of mathematical simplifications to

the rotating thermal convection problem follow from taking this limit of vanishing centrifugal buoyancy.

The centrifugal buoyancy drives a large-scale circulation in which the cool denser fluid is centrifuged radially outward and the hot less-dense fluid is centrifuged radially inward (Barcilon & Pedlosky 1967; Homsy & Hudson 1969; Hart 2000). This large-scale circulation exists for any non-zero difference in temperature between the top and bottom plate, and so there is no trivial conduction state when the centrifugal buoyancy is incorporated. Neglecting the centrifugal buoyancy allows a straightforward linear stability analysis for the onset of convection from the conduction state; Chandrasekhar (1961) provides a comprehensive account of this when the fluid layer is assumed to be horizontally unbounded. In the horizontally unbounded case, Küppers & Lortz (1969) found a new mode of instability where convection rolls become unstable to another set of rolls aligned at a different angle (whose value depends on parameters). This instability leads to chaotic flow very near the onset of convection and has led to many experimental investigations in large-aspect-ratio containers as well as theoretical investigations in terms of reduced models and Ginsburg–Landau equations (see Knobloch 1998; Bodenschatz, Pesch & Ahlers 2000, for reviews).

There had been problems in reconciling experimental data in finite though large-aspect-ratio containers and the unbounded theory (e.g. Rossby 1969; Pfotenhauer, Niemela & Donnelly 1987; Bajaj *et al.* 1998), and it was concluded that lateral boundaries change the picture considerably. A linear stability analysis neglecting centrifugal buoyancy in an enclosed rotating cylinder shows that when the system is rotating sufficiently fast, the onset of thermal convection from the conduction state is to a so-called wall mode which consists of alternating hot and cold thermals rising and descending in the cylinder boundary layer and precessing retrograde with respect to the rotation of the cylinder (Goldstein *et al.* 1993); Buell & Catton (1983) noted the spatial structure of these wall modes earlier, but assumed that they were a stationary mode and missed the fact that they precess. These linear stability analyses are still relatively straightforward since the state whose stability is being tested is the trivial conduction state. Experiments to test this linear theory have needed to be carefully designed in order to minimize the effects of the neglected centrifugal buoyancy, and have found good agreement with the theory for the onset of convection (Zhong, Ecke & Steinberg 1991, 1993; Ning & Ecke 1993; Liu & Ecke 2002). More recently, nonlinear computations neglecting centrifugal buoyancy have found good agreement with the very low centrifugal buoyancy experiments (Rüdiger & Knobloch 2003; Sánchez-Álvarez *et al.* 2005). Nevertheless, the question still remains as to what are the effects of centrifugal buoyancy on thermal convection and when is it safe to neglect centrifugal buoyancy.

The presence of centrifugal buoyancy changes the problem in a fundamental manner. The total buoyancy force (gravitational plus centrifugal) no longer points solely in the vertical direction, but now also has a radial component which varies with radial distance from the rotation axis. This destroys the horizontal translation invariance that is inherent in the unbounded theoretical treatments of the problem. Furthermore, the reflection symmetry about the cylinder mid-height is also destroyed. When the centrifugal buoyancy is small, it acts like an imperfection to the symmetric problem, and has some analogies with the Taylor–Couette problem between finite-length cylinders (Benjamin 1978*a*,*b*; Benjamin & Mullin 1981). When the centrifugal buoyancy is neglected, the onset of convection is via a pitchfork bifurcation when the system is further restricted to an axisymmetric subspace, giving two steady

convecting states that are reflections of each other (of course, over a wide range of parameter space with a sufficiently strong Coriolis force acting, the conduction state is first unstable to the non-axisymmetric wall modes, but the underlying axisymmetric pitchfork bifurcation is essential to the complete picture). Centrifugal buoyancy renders the pitchfork bifurcation imperfect, resulting in two distinct branches of (axisymmetric) steady states that are not related by any symmetry. One is the smooth connection to the large-scale circulation driven by the centrifugal buoyancy and the other comes into existence at a saddle-node bifurcation when the gravitational buoyancy is of sufficient strength. Additional axisymmetric branches appear in saddle-node bifurcations, differing in the number of circular concentric roll cells. How the centrifugal buoyancy and the gravitational buoyancy interact and compete is different along each branch.

In order understand the effects due to the centrifugal buoyancy, it is first necessary to understand how it affects the axisymmetric states. The spatial structure of convective axisymmetric states consists of steady concentric rolls, the so-called target patterns. Koschmieder (1967), in an early experiment on the onset of rotating convection in a large-Prandtl-number fluid, observed that these types of axisymmetric patterns are initiated near the cylinder sidewall. Although for most of parameter space these axisymmetric ring modes are unstable, they have also been observed experimentally either as transient states or by forcing them to be stable. The early experiments of Koschmieder (1968) attempted to stabilize the concentric rolls by non-uniformly heating the bottom plate. For zero rotation, Hu, Ecke & Ahlers (1993) and Royer *et al.* (2004) stabilized the target patterns by applying a small static heat source at the sidewall. In a rotating system, Thompson, Bajaj & Ahlers (2002) were able to stabilize the axisymmetric rolls by weakly modulating the rotation of the cylinder.

We have observed that in the axisymmetric subspace steady target patterns are unstable to a radial travelling wave mode where the axisymmetric rolls propagate radially inward in a periodic fashion, much like the computed axisymmetric travelling waves found by Tuckerman & Barkley (1988) in a non-rotating system with a non-insulating sidewall. These radially travelling target patterns have also been stabilized experimentally by suitably modulating the rotation (Thompson *et al.* 2002). In this paper, we enforce axisymmetry. This restriction enables a computationally tractable systematic study of the influence of the centrifugal force on rotating Rayleigh–Bénard convection and allows us to explore in detail the generation and dynamics of the travelling wave states, and how centrifugal buoyancy affects them.

2. Governing equations

We consider the flow in a circular cylinder of radius r_0 and depth d, rotating at a constant rate ω rad s^{-1}. The top endwall is maintained at a constant temperature $T^* = T_0 - 0.5\Delta T$ and the bottom endwall at a constant temperature $T^* = T_0 + 0.5\Delta T$. The Boussinesq approximation is implemented, which treats all fluid properties as constant, except for the density in the buoyancy terms which are composed of the gravitational and the centrifugal buoyancies. To lowest order, the density varies linearly with temperature, i.e.

$$\rho = \rho_0(1 - \alpha(T^* - T_0)), \tag{2.1}$$

where T_0 is the mean temperature and ρ_0 is the density at that temperature. In the

rotating frame of reference, the governing equations are

$$(\partial_t + \boldsymbol{u}\cdot\nabla)\boldsymbol{u} = -\nabla P/\rho_0 + \nu\nabla^2\boldsymbol{u} + g\alpha T\hat{\boldsymbol{z}} + 2\omega\boldsymbol{u}\times\hat{\boldsymbol{z}} - \omega^2\alpha T\boldsymbol{r}, \tag{2.2}$$

$$(\partial_t + \boldsymbol{u}\cdot\nabla)T = \kappa\nabla^2 T, \tag{2.3}$$

$$\nabla\cdot\boldsymbol{u} = 0, \tag{2.4}$$

where $\boldsymbol{u}$ is the velocity field, $T = T^* - T_0$ is the temperature deviation with respect to the mean temperature T_0, P is the dynamic pressure which incorporates the hydrostatic pressure due to the gravitational and centrifugal forces, g is the gravitational acceleration, α is the coefficient of volume expansion, ν is the kinematic viscosity, and κ is the thermal diffusivity.

The system is non-dimensionalized using d as the length scale, d^2/κ as the time scale, and ΔT as the temperature scale. There are five non-dimensional parameters:

Rayleigh number:	$R = \alpha g d^3\Delta T/\kappa\nu$,
Coriolis number:	$\Omega = \omega d^2/\nu$,
Froude number:	$F = \omega^2 r_0/g$,
Prandtl number:	$\sigma = \nu/\kappa$,
aspect ratio:	$\gamma = r_0/d$.

Restricting the system to an axisymmetric subspace, the non-dimensional governing equations reduce to

$$\mathrm{D}v - \frac{2\sigma\Omega}{r}\psi_z - \frac{v}{r^2}\psi_z = \sigma\left(\partial_z^2 + \partial_r^2 + \frac{1}{r}\partial_r - \frac{1}{r^2}\right)v, \tag{2.5}$$

$$\mathrm{D}\eta + \frac{\eta\psi_z}{r^2} - \frac{2}{r}vv_z - 2\Omega\sigma v_z = \sigma R\left(-T_r - \frac{F}{\gamma}rT_z\right) + \sigma\left(\partial_z^2 + \partial_r^2 + \frac{1}{r}\partial_r - \frac{1}{r^2}\right)\eta, \tag{2.6}$$

$$\mathrm{D}T = \left(\partial_z^2 + \partial_r^2 + \frac{1}{r}\partial_r\right)T, \tag{2.7}$$

where $\mathrm{D} = \partial_t + 1/r(\psi_r\partial_z - \psi_z\partial_r)$, the velocity is written in terms of a streamfunction $(u, v, w) = (-\psi_z/r, v, \psi_r/r)$, and η is the azimuthal component of vorticity satisfying

$$\left(\partial_z^2 + \partial_r^2 - \frac{1}{r}\partial_r\right)\psi = -r\eta. \tag{2.8}$$

The boundary conditions are:

$$r = 0: \qquad T_r = v = \psi = \psi_r = 0; \tag{2.9}$$

$$r = \gamma: \qquad T_r = v = \psi = \psi_r = 0; \tag{2.10}$$

$$z = \pm 0.5: \qquad T = \mp 0.5,\ v = \psi = \psi_z = 0. \tag{2.11}$$

Equations (2.5)–(2.8) are solved on a uniform grid using second-order centred-differences in space and a second-order explicit predictor–corrector scheme in time. The same code has been used to study the effects of centrifugal buoyancy for the stably stratified case (Brummell, Hart & Lopez 2000). Here, we have fixed $\gamma = 4$, $\sigma = 7$, and $\Omega = 625$, and consider variations in R and F. We have used 101 grid points in z and 401 grid points in r and a time step $\mathrm{d}t = 2.3\times10^{-6}$ thermal time units.

Apart from being restricted to the axisymmetric subspace, the system, in the limit $F \to 0$, has an additional symmetry. The governing equations and boundary

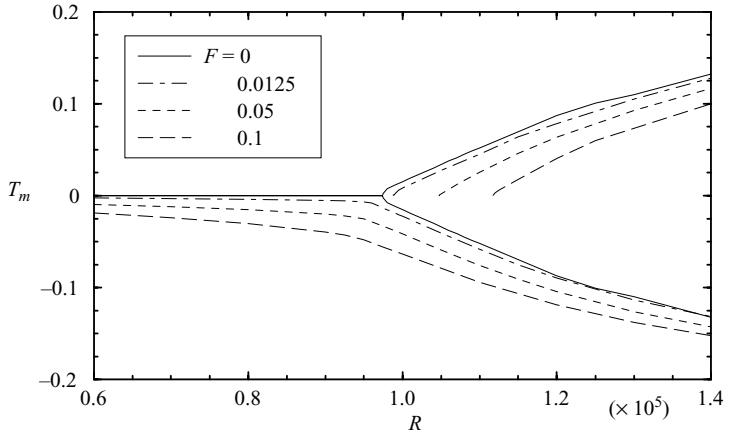

FIGURE 1. Variation with R of the temperature at the sidewall at mid-height, T_m, for various values of F as indicated.

conditions are reflection-symmetric about the cylinder half-height. The action, K, of this Z_2 symmetry on the flow is

$$K(\psi, v, \eta, T)(r, z) = (-\psi, v, -\eta, -T)(r, -z). \tag{2.12}$$

3. Results

3.1. *Onset of convection*

For small R, the only solution with $F = 0$ is a conducting state with zero relative velocity and a linear vertical temperature gradient, $T = -z$. This conduction state loses stability for $R > R_c(\sigma, \gamma, \Omega)$ via a pitchfork bifurcation. In this paper, we fix $\gamma = 4$, $\sigma = 7$ and $\Omega = 625$. For these values, $R_c \approx 9.85 \times 10^4$. For comparison, steady rotating Rayleigh–Bénard convection between rigid plates in a horizontally unbounded domain with $\Omega = 625$ (which corresponds to a Taylor number $Ta = 4\Omega^2 = 1.56 \times 10^6$) sets in at $R_c \approx 9.2 \times 10^4$ with critical wavenumber $a_c \approx 11.8$ (see figures 21 and 22 in Chandrasekhar 1961); note that this classical linear stability result is for $F = 0$ and $\gamma \to \infty$ and is independent of σ. From our figure 2, the radial wavenumber of the circular cells is $2\pi \times 7.5/\gamma = 11.78$ which is in very good agreement with the classical theory, suggesting that the circular concentric rolls are the analogues of the planar two-dimensional convection rolls. The critical R in the enclosed cylinder is a little larger than in the unbounded system, and this is to be expected due to the presence of the no-slip cylinder wall. At the pitchfork bifurcation, two branches of steady symmetrically related solutions are created. Figure 1 is a bifurcation diagram using the temperature at mid-height on the sidewall, $T_m = T(r = \gamma, z = 0)$, as the measure of the flow state. The stable conduction state and the symmetrically related steady convection states, for $F = 0$, are the solid curves. The convecting solutions are cellular in character, having either eight warm plumes rising and seven cold plumes falling or seven warm plumes rising and eight cold plumes falling. For R just above R_c these plumes are small in amplitude and grow with increasing R. Figure 2 shows contours of the streamfunction ψ, temperature deviation T, relative angular momentum rv, and azimuthal vorticity η at $R = 10^5$ for the cellular states on the two branches of the

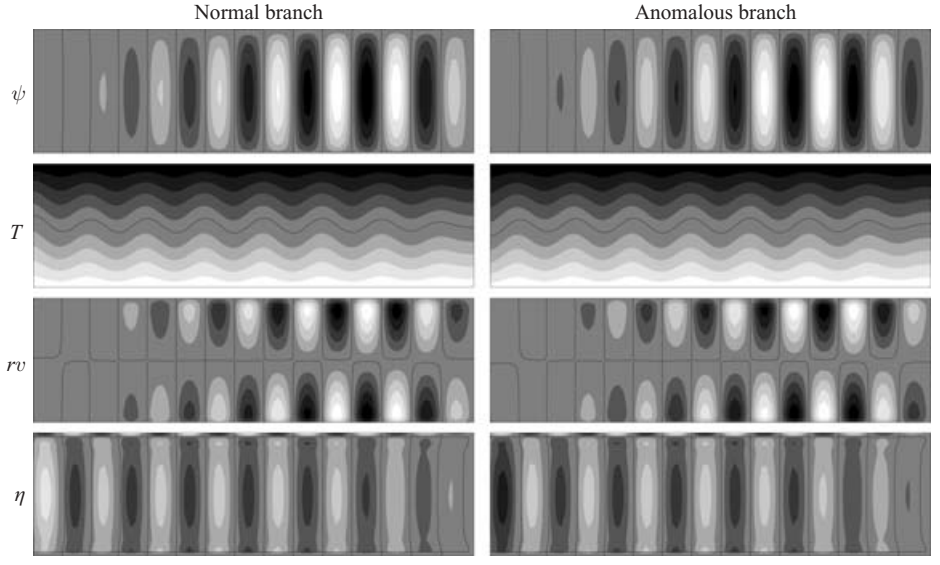

FIGURE 2. Contours of ψ, T, rv and η on the normal (left) and anomalous (right) branches for $F = 0$ and $R = 10^5$. Contour levels (grey scales) are evenly spaced with $\psi \in [-7.9\times10^{-3}, 7.9\times10^{-3}]$, $T \in [-0.5, 0.5]$, $rv \in [-2.4, 2.4]$, and $\eta \in [-220, 220]$. The black curves are the zero contours, the darker (lighter) grey scales are negative (positive). For each panel, the left vertical boundary is the axis $r = 0$, the right vertical boundary is the cylinder wall $r = \gamma$, and the top and bottom boundaries are the plates at $z = +0.5$ and $z = -0.5$, respectively.

pitchfork. This value of R is just slightly above critical ($\epsilon \equiv (R - R_c)/R_c \approx 0.015$). We name the branch with cold fluid flowing down the sidewall 'normal' and the one with warm fluid flowing up the sidewall 'anomalous'. For $F = 0$, this distinction in not very meaningful, but when $F \neq 0$, the centrifugal buoyancy favours the normal state with cold fluid being centrifuged out and consequently flowing down the sidewall. We introduce a naming convention for these cellular states. The first letter in the name is either N (for normal) or A (for anomalous) corresponding to states with either a cold downdraught or a warm updraught on the sidewall, followed by the number of warm plumes rising across the radius, and then either H or C for a rising hot plume or a descending cold plume on the axis. The states shown in figure 2, using this naming convention are N8H and A8C. That the solutions on the two branches are K-conjugates for $F = 0$ is apparent in the figure.

We have used the term cellular for the steady states because there are zero streamlines beginning and ending on the top and bottom endwalls that follow the centres of the ascending warm plumes and descending cool plumes. There is no fluid transport across these streamlines and hence the flow is confined to cells in between them. At first glance it appears that the radial extent of these (circular) cells is approximately constant. However, closer inspection of, say, the results in figure 2 with $R = 10^5$ and $F = 0$, shows that this is only approximately so for R near R_c; as R increases the states have fewer plumes and the variation amongst them is more evident (both when $F = 0$ and $F \neq 0$). It needs to be noted that the radial direction is not a periodic direction. Apart from the fact that the boundary conditions for the velocity at $r = \gamma$ are rigid no-slip, there is also the presence of curvature which would destroy radial invariance even for $\gamma \to \infty$. Even for $R \sim R_c$ where the radial extent

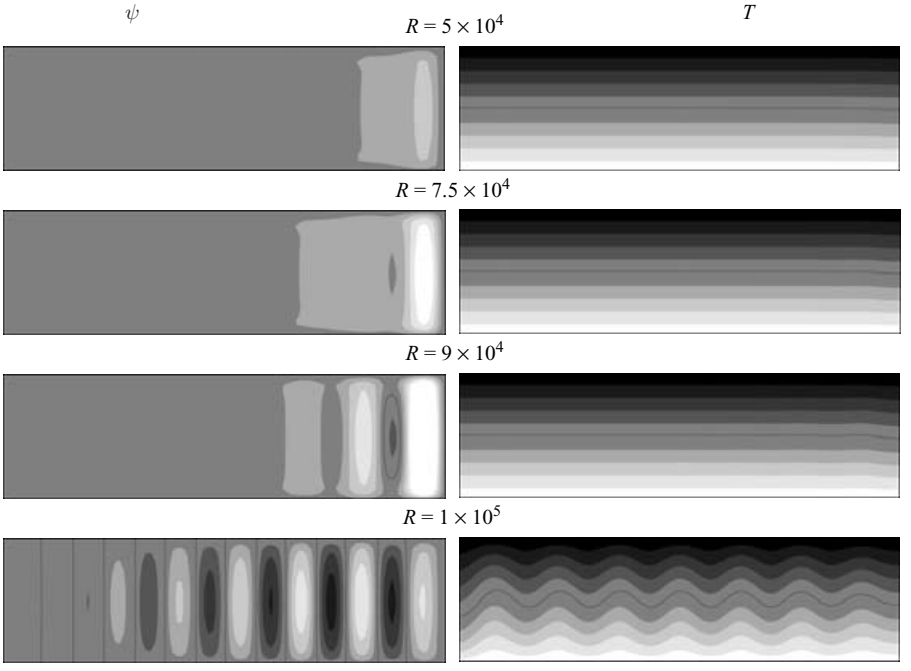

FIGURE 3. Streamlines and temperature contours for normal branch solutions at $F = 0.05$, for R values as indicated. ψ-contours are evenly spaced between $[-0.011, 0.011]$ for $R = 5 \times 10^4$, 7.5×10^4 and 9×10^4 and between $[-0.11, 0.11]$ for $R = 1 \times 10^5$.

of each cell is very nearly the same, the cells contain different volumes of fluid due to the curvature. These considerations make the presence of radially travelling waves all the more remarkable (these are described in §3.3).

The (weak) ascending thermal plumes associated with the cellular convection states in figure 2 drive clockwise meridional circulations with $\psi > 0$ on the large-r sides of the plumes and counterclockwise circulations with $\psi < 0$ on the small-r sides of the plumes (both when $F = 0$ and $F \neq 0$). Near the top and bottom of the cylinder, these cellular circulations are predominantly in the radial direction. In regions where the radial velocity, $u = -\psi_z/r$, is positive, fluid with axial angular momentum rv is advected to larger r and is consequently spun-down, whereas where u is negative, the flow is spun-up. This ballerina effect is evident in the contours of rv in figure 2.

When the contributions of the centrifugal force to the rotation are accounted for ($F > 0$), no conduction state exists for any $R > 0$. Instead, at low R a large-scale circulation centrifuges the cool (relatively dense) fluid near the top radially outward and warmer fluid near the bottom is drawn radially inward. This results in a cold downdraught in the sidewall boundary layer generating a localized recirculation zone that smoothly develops into a cellular structure of concentric rings as R is increased past R_c. Figure 3 shows such a smooth development from the large-scale circulation at $R = 5 \times 10^4$ through to the cellular state at $R = 10^5$ for small $F = 0.05$. This concentric ring state is similar to the $F = 0$ state at $R = 10^5$ (see figure 2) with seven rising warm plumes and eight descending cold plumes, but there are differences. The $F = 0$ state is N8H and the $F = 0.05$ state is N7C. We have found that there is a hysteretic switch between N8H and N7C for $R \in (1.1 \times 10^5, 1.2 \times 10^5)$ when $F = 0$. The hysteretic pattern selection is discussed below in §3.2.

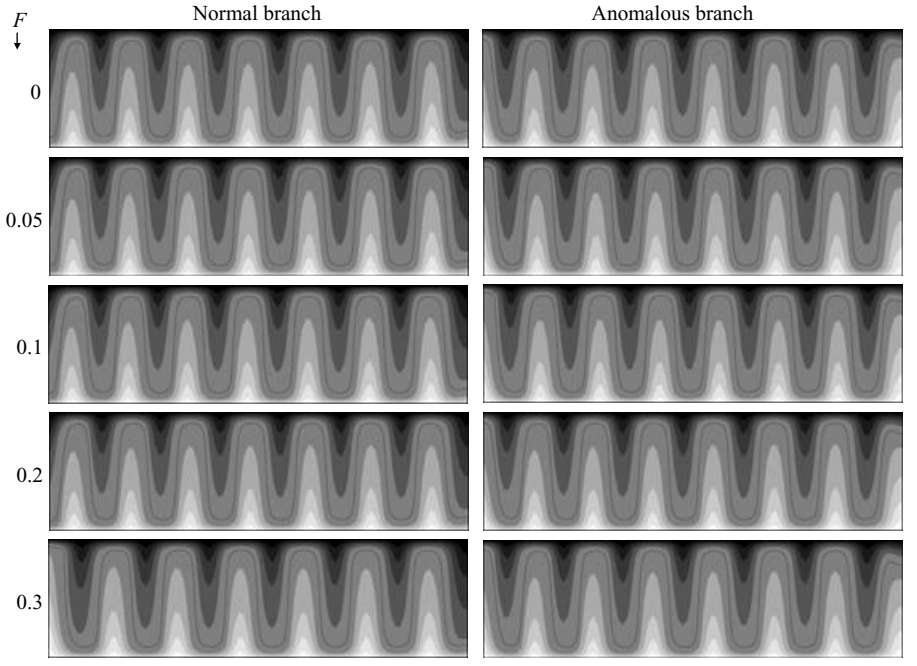

FIGURE 4. Isotherms of the steady states along the normal and anomalous branches for $R = 2.5 \times 10^5$, $\sigma = 7.0$, $\gamma = 4.0$, $\Omega = 625$ and F as indicated.

The smooth transition from the large-scale circulation to the concentric ring pattern shown in figure 3 is consistent with the onset of thermal instability in a rotating cylinder observed in the experiments of Koschmieder (1967) and with the asymptotic calculations of Daniels (1980), who also observed that axisymmetric convection sets in at large radius with more and more circular cells filling radially inward with increasing R.

The Froude number F, parameterizing the centrifugal buoyancy, acts as an imperfection parameter unfolding the pitchfork bifurcation for the onset of convection (see figure 1). The normal branch from the $F = 0$ pitchfork with the cool downdraft on the sidewall becomes the $F \neq 0$ branch smoothly connected to the large-scale circulation as $R \to 0$. The $F = 0$ pitchfork branch with the warm updraft on the sidewall is the disconnected anomalous branch for $F \neq 0$. This branch comes into existence at a saddle-node bifurcation at $R_{\rm sn} > R_{\rm c}$, where the value of $R_{\rm sn}$ increases with F. Note that the mid-height sidewall temperature is cooler for larger F on both branches; the centrifugally driven large-scale circulation enhances the cool downdraft on the normal branch and opposes the warm updraft on the anomalous branch, i.e. on the normal branch the effects of centrifugal and gravitational buoyancy reinforce each other whereas on the anomalous branch they oppose each other. Figure 4 shows isotherms for solutions on both branches, side-by-side, at the same points in parameter space. For small $F \lesssim 0.2$, we have $T(r, z) \approx -T(r, -z)$. However, for $F = 0.3$ there are large differences on the two branches, in particular both have a hot plume rising on the axis.

3.2. *Pattern selection*

As is evident from the results presented so far, there are multiple co-existing stable solutions over a considerable range of parameters. We have found that stable steady

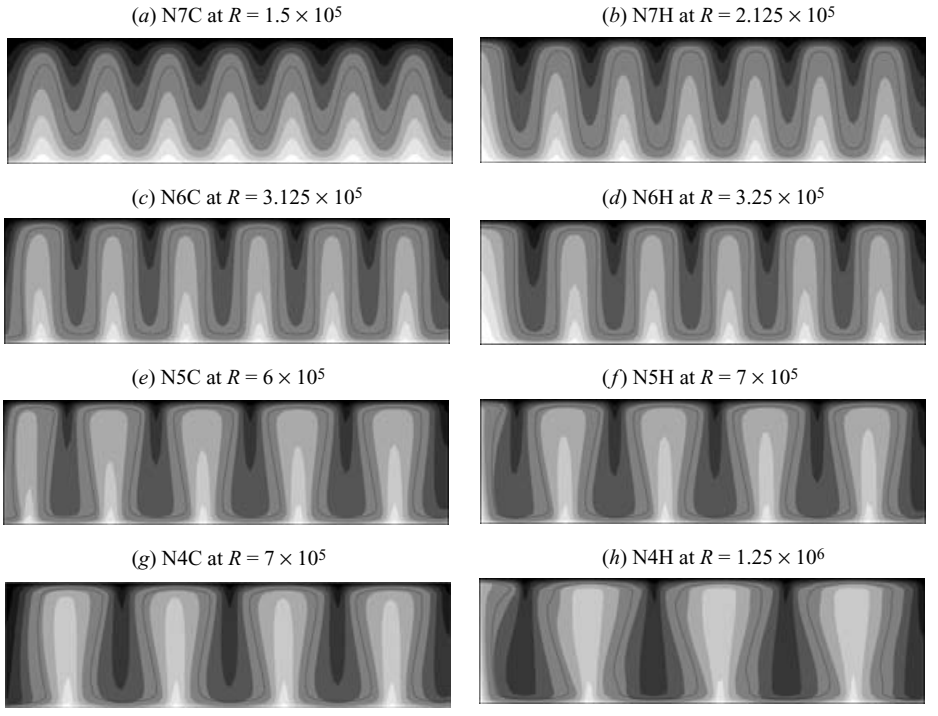

FIGURE 5. A selection of different patterns for the $F = 0.3$ normal branch.

cellular states either bifurcate directly from the conduction state when $F = 0$ via a pitchfork bifurcation, or are created and destroyed at saddle-node bifurcations. That the bifurcations are steady for the parameter regimes we have considered is a consequence of the restriction to an axisymmetric subspace; without this restriction for the $F = 0$ case it is well-known that the conduction state first loses stability via a Hopf bifurcation to a precessing wall mode. Since we have only varied R and F, we only have one pair of symmetrically related stable states emerging at the pitchfork bifurcation when $F = 0$. All the other $F = 0$ states we have found, like the $F \neq 0$ states, are created and destroyed at saddle-node bifurcations.

At a given point in parameter space, we have found up to four stable distinct cellular states. The various coexisting states have been found by starting the computations with different initial conditions, and the branches of each of these are found by continuation (using the solution at one value of R as initial condition for a slightly different value of R). The branches are terminated at saddle-node bifurcations, and the continuation strategy leads to a 'switching' to another branch. For $\gamma = 4$, $\sigma = 7$ and $\Omega = 625$ the cellular states for small F and $R \sim R_c$ are N8H on the normal branch and A8C on the anomalous branch. As either F or R is increased, there is a tendency to switch to states with fewer plumes (i.e. with larger radial wavelength). This trend for increasing R with fixed $F = 0.3$ along the normal branch is illustrated in figure 5, which shows isotherms of the various cellular states encountered: N7C $\rightarrow$ N7H $\rightarrow$ N6C $\rightarrow$ N6H $\rightarrow$ N5C $\rightarrow$ N5H $\rightarrow$ N4C $\rightarrow$ N4H. Figure 6 illustrates the switching from N7C to N7H, from N7H to N6C, and from N6C to N6H via saddle-node bifurcations as R is increased for $F = 0.3$ in terms of T_m, giving a clear indication of the hysteretic overlap regions between adjacent cellular states.

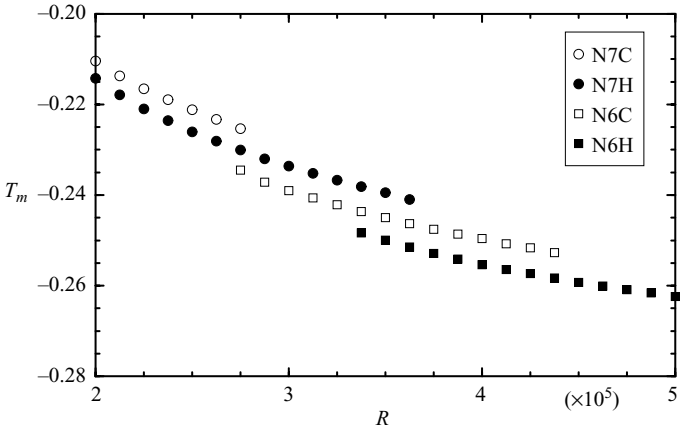

FIGURE 6. Switching via saddle-node bifurcations between cellular patterns on the normal branch with $F = 0.3$.

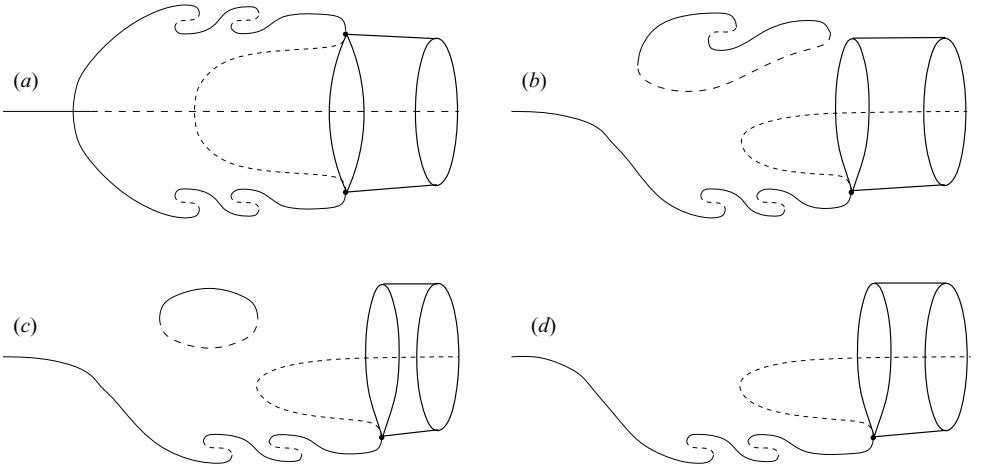

FIGURE 7. Schematics of the unfolding of the pitchfork bifurcation for various F; the horizontal axis is R and the vertical axis is a measure of the flow state (e.g. temperature at a point): (*a*) the symmetric case at $F = 0$, (*b*) and (*c*) increasing Froude numbers, and (*d*) by further increasing F, the anomalous branch disappears in an isola bifurcation. The solid (dashed) lines are stable (unstable) steady states; the thick lines correspond to limit cycles, that appear in SNIC bifurcations.

Figure 7 is a sequence of schematic bifurcation diagrams for various F; the horizontal axis is R and the vertical axis is a measure of the flow state (e.g. temperature at a point). It is a summary of our results such as in figure 6 showing the hysteretic (with varying R) coexisitence of states with differing numbers of rolls. Part (*a*) is for $F = 0$ showing the first pitchfork bifurcation from the conduction state at $R = R_c$ and the hysteretic regions in between the saddle-node bifurcations. The steady-state branches are terminated by saddle-node bifurcations which we conjecture to involve an unstable (saddle) pair of symmetrically related states that originate at a pitchfork bifurcation from the unstable conduction state at $R > R_c$. These saddle-node bifurcations are special as they lead to the creation of a time-periodic state, which we describe in detail in §3.3, due to a global reconnection between them. The bifurcation is a saddle-node on an invariant circle (SNIC), where after the bifurcation

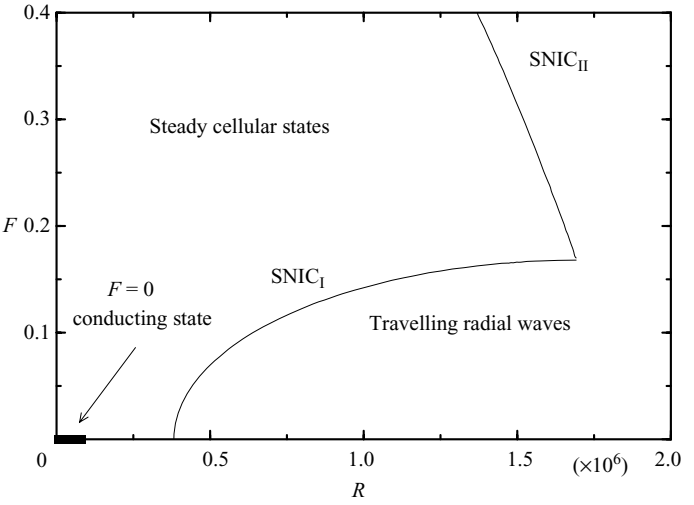

FIGURE 8. The location in (R,F) parameter space of the SNIC bifurcation curves that give rise to travelling waves of modes I and II. The intersection of the two bifurcation curves is a cusp point near ($R = 1.69 \times 10^5$, $F = 0.168$).

the stable and unstable manifolds connecting the saddles and nodes, which have annihilated each other, persist as a limit-cycle solution.

The others parts of figure 7 correspond to increasing $F > 0$. Part (b) is for small F and simply corresponds to an unfolding of the symmetric picture in part (a). The unfolding of the unstable pitchfork (dashed curves) is conjectured, but we have direct numerical evidence of the unfolding of the stable branches: in particular how the anomalous branch begins at a saddle-node bifurcation for $R = R_{sn} > R_c$ with R_{sn} increasing with F, as illustrated in parts (c) and (d) of the figure, and terminating at an ordinary saddle-node bifurcation at larger R. The value of R for this terminal saddle-node bifurcation decreases with F so that for $F \sim 0.2$ the anomalous branch vanishes in an isola (i.e. the saddle-nodes that delimit the anomalous branch collapse in on themselves as F increases beyond about 0.2).

3.3. *Travelling waves*

As illustrated schematically in figure 7, the normal branch of steady solutions is terminated at a SNIC bifurcation leading to time-periodic flow. For the parameter regime considered ($\gamma = 4$, $\Omega = 625$, $\sigma = 7$), the loci of this bifurcation in (R, F)-parameter space is plotted in figure 8. In fact, we have found two distinct curves of SNIC bifurcations, labelled SNIC$_I$ and SNIC$_{II}$, which come together at a cusp-like point at $R \approx 1.69 \times 10^6$, $F \approx 0.168$. Note that this cusp-like intersection of two SNIC curves is very different from the conventional codimension-two cusp point where two curves of regular saddle-node bifurcations meet. In that case, the two steady states that are created at each of the saddle-node bifurcations coexist and are stable inside the cusp region. In our problem, outside the cusp region (to the right of the SNIC$_I$ and SNIC$_{II}$ curves) we have time-periodic states while inside the cusp region there are only steady states.

Figure 9 shows the variations with R of the period, τ, of the oscillatory states as (a) the SNIC$_I$ curve is crossed with $F = 0$ and (b) the SNIC$_{II}$ curve is crossed with $F = 0.3$. In both cases, as $R \to R_{SNIC}$ from above, the period becomes unbounded following the characteristic $(R - R_{SNIC})^{-0.5}$ scaling associated with a SNIC bifurcation.

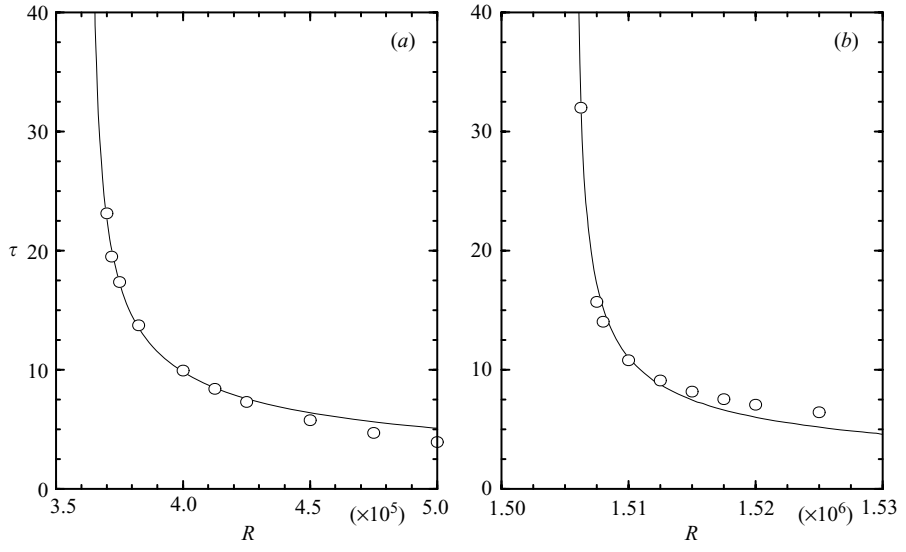

FIGURE 9. Periods in thermal time units vs. R for (*a*) $F = 0$ and (*b*) $F = 0.3$. The curve is of the form $(R - R_{\mathrm{SNIC}})^{-0.5}$ fitted to the first four data points of each case.

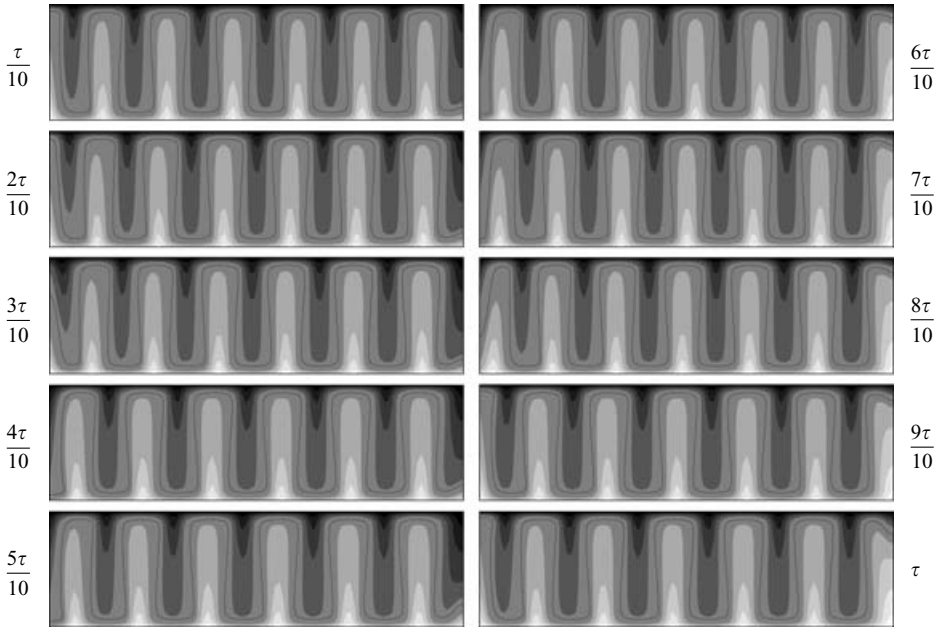

FIGURE 10. Isotherms at equally spaced times over one period, $\tau \approx 9.9$, of an oscillatory state at $R = 4 \times 10^5$, $F = 0$.

At $F = 0$, the SNIC bifurcation breaks the spatial K-reflection symmetry, but the resulting limit cycle retains a spatio-temporal Z_2 symmetry, H, whose action is

$$H(\psi, v, \eta, T)(r, z, t) = (-\psi, v, -\eta, -T)(r, -z, t + \tau/2) = (\psi, v, \eta, T)(r, z, t). \quad (3.1)$$

Figure 10 shows isotherms at 10 equally spaced phases over one oscillation period τ of the symmetric limit cycle at $F = 0$, $R = 4 \times 10^5$ (which is a little beyond the

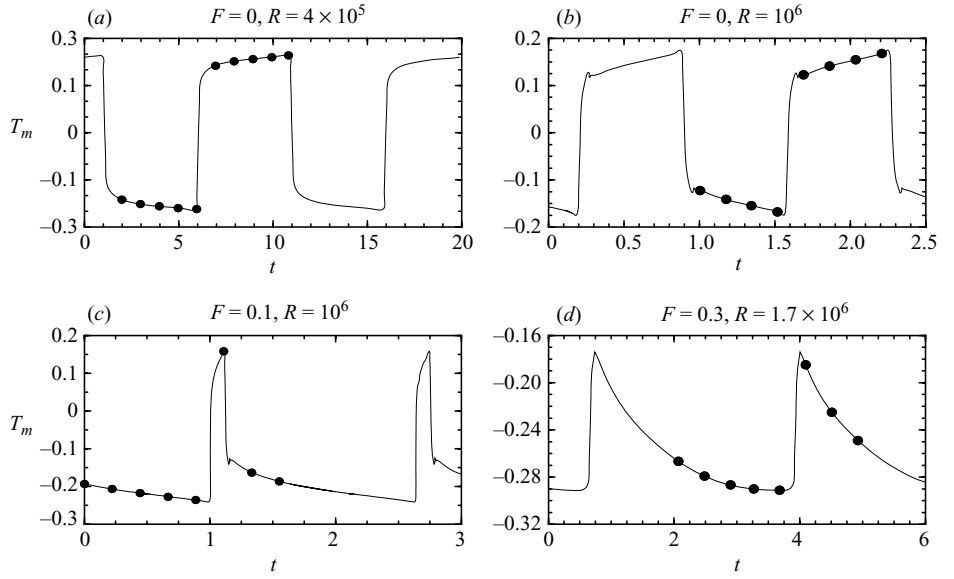

FIGURE 11. Time-series of the temperature on the sidewall at mid-height, T_m, over approximately two oscillation periods for each case (F and R as indicated). The symbols indicate times corresponding to the isotherm plots in figures 10–15.

critical $R_{\mathrm{SNIC}} \approx 3.65 \times 10^5$). The H-symmetry is evident from comparing isotherms half a period apart and noting that $T(r, z, t) = -T(r, -z, t + \tau/2)$. The limit cycle is far from being a uniform oscillator, as it would be if it had originated at a Hopf bifurcation, due to its creation via a SNIC bifurcation. The limit cycle has the characteristic slow–fast oscillations, spending a long time in the neighbourhood of the ghost of the saddle-node (there are two due to the Z_2 nature of the H-symmetry, corresponding to the saddle-nodes on the anomalous and the normal branches), and then rapid excursions from one ghost to the other. The time-series of the mid-height sidewall temperature deviation, T_m, shown in figure 11(a) illustrates this slow–fast oscillation with $T_m(t) = -T_m(t + \tau/2)$. The symbols on the time-series plot correspond to the isotherms in figure 10. The left-hand column of isotherms correspond to the $T_m < 0$ phase of the oscillation with a cold plume descending on the sidewall and the right-hand column to the $T_m > 0$ phase with a warm plume on the sidewall. Notice that during the first phase, there is a warm plume on the axis which is quenched by the surrounding cold plume closing in on it, and at the end of this phase, the rapid excursion seen in the T_m time-series corresponds to a new warm plume being created at the sidewall. If we were to record T at the mid-height on the axis, we would have a time-series similar to that on the sidewall but shifted by $\tau/4$. This is best illustrated in a space–time diagram of $T(r, z = 0, t)$. Figure 12(a) is such a diagram for $F = 0$, $R = 4 \times 10^5$. The figure extends over about 1.6 periods. It shows that the creation of plumes at the sidewall and the quenching of plumes at the axis occur very rapidly and that the plumes travel radially inward rather slowly (taking about five oscillation periods, which is about 80 thermal time units, to travel from $r = \gamma$ to $r = 0$). The plumes, away from the sidewall and the axis, travel at a fairly uniform speed without much distortion to their (r, z) structure.

For larger $R = 10^6$, the oscillation period reduces considerably, but the oscillation retains its slow–fast character (see figure 11b). The plumes created at the sidewall are

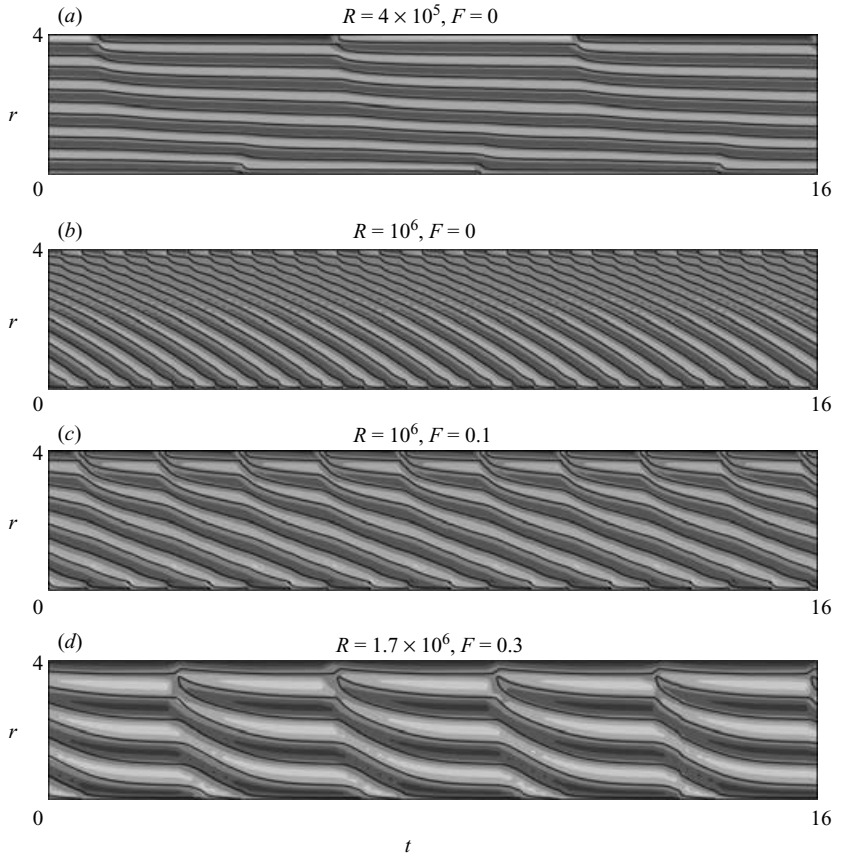

FIGURE 12. Space–time diagrams of the temperature at mid-height $z = 0$ for R and F as indicated; the contour line corresponds to $T = 0$, the dark shades are for $T \in [-0.5, 0]$ and the light shades for $T \in [0, 0.5]$.

considerably thinner and travel into the interior faster, and as they do they broaden their radial extent (see figure 13, which also shows that this oscillatory state is H symmetric). As they approach the axis, they speed up as they quench the plume on the axis. The non-uniform speed of propagation is clearly evident in the space–time diagram of figure 12(b).

When $F \neq 0$, the H-symmetry is broken, but for small $F > 0$ it is only weakly broken and we have an unfolding of the H-symmetric SNIC bifurcation, as illustrated in figure 7. With $F = 0$, the oscillation is a symmetric switching between a cold plume descending and a warm plume ascending on the sidewall. With $F \neq 0$, the large-scale circulation associated with the centrifugal buoyancy favours the cold plume on the sidewall phase of the oscillation, and so that phase is longer than the phase with the warm plume on the sidewall. Figure 11(c) illustrates this effect for $F = 0.1$, $R = 10^6$. The period of the oscillation is about the same as for the $F = 0$, $R = 10^6$ case shown in figure 11(b) ($\tau \approx 1.3$), but the $T_m < 0$ phase is about 0.9τ when $F = 0.1$. The structure of the plumes have not been altered in any significant way by having small $F > 0$ (compare figures 13 and 14, both at $R = 10^6$ but one at $F = 0$ and the other at $F = 0.1$), but their propagation characteristics certainly have. The corresponding space–time diagram, figure 12(c), shows that a warm plume is created on the sidewall

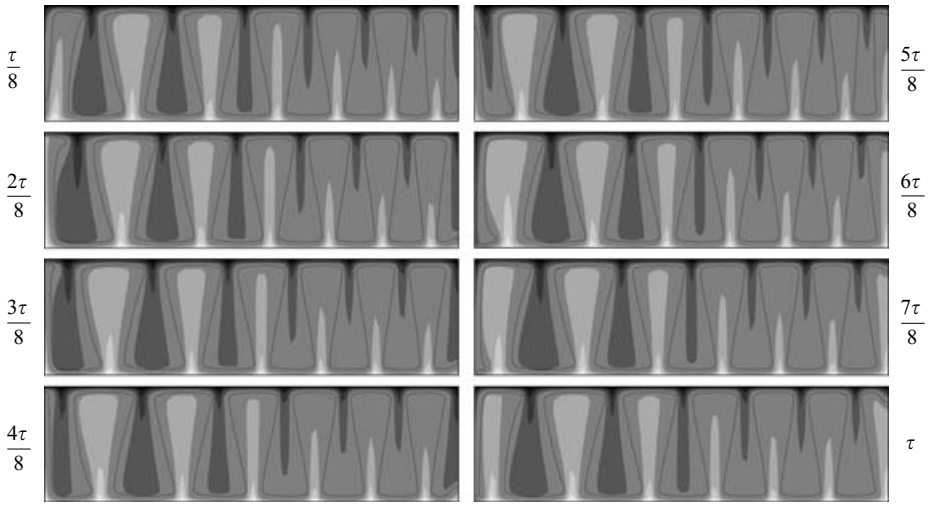

FIGURE 13. Isotherms at equally spaced times over one period, $\tau \approx 0.9$, of an oscillatory state at $R = 10^6$, $F = 0$.

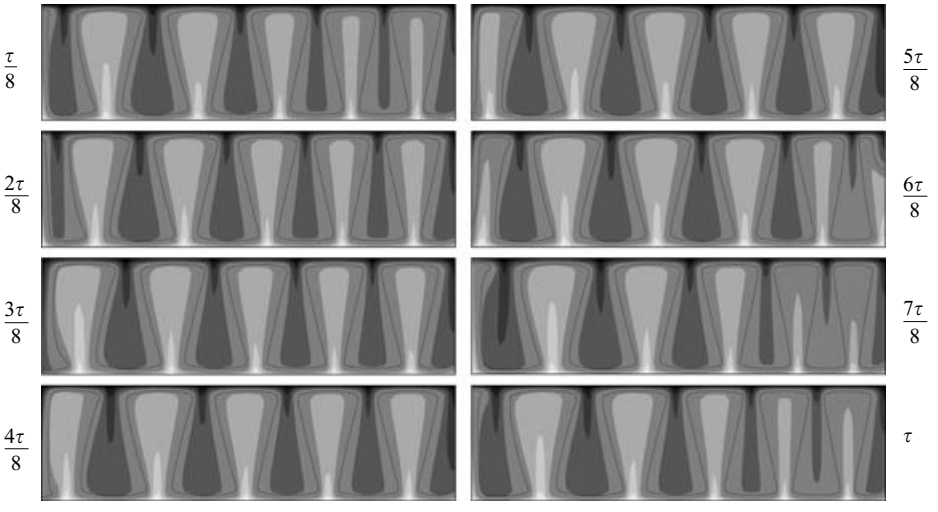

FIGURE 14. Isotherms at equally spaced times over one period, $\tau \approx 1.7$, of an oscillatory state at $R = 10^6$, $F = 0.1$.

and is almost immediately pushed in by the creation of a cold plume. This pair remain almost stationary until a new warm plume is created and they begin a fairly uniform-speed propagation in toward the axis. The quenching of either cold or hot plumes on the axis is quite uniform, each taking about $\tau/2$ to be quenched.

For $F > 0.17$, the nature of the oscillation changes, as illustrated schematically in figure 7, due to the centrifugal buoyancy being too strong at the sidewall to allow the formation of a warm plume there. For the higher F cases, the sidewall always has a cold plume descending and the oscillation corresponds to the adjacent warm plume splitting into two and then all but the outermost warm plume propagating radially inward. For these cases, the propagation speed is much less uniform and the plumes shuffle inward in fits and starts. The quenching of the cold plume on the axis is much faster than the quenching of the warm plume on the axis. We interpret this as being

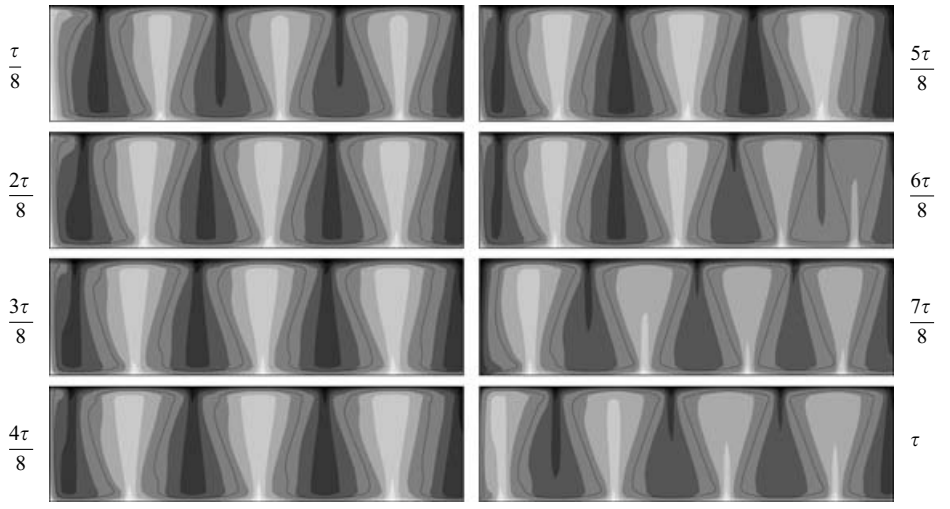

FIGURE 15. Isotherms at equally-spaced times over one period, $\tau \approx 3.3$, of an oscillatory state at $R = 1.7 \times 10^6$, $F = 0.3$.

a consequence of the centrifugal large-scale circulation which favours a warm plume ascending on the axis. All of these processes are illustrated in figures 15 and 12(*d*). The time-series of T_m (figure 11*d*) shows that there is only a $T_m > 0$ phase to the large-F oscillation.

4. Discussion and conclusions

While stationary concentric ring patterns have been observed in many experiments in circular cylinders of a variety of aspect ratios using fluids with a wide range of Prandtl numbers, and both with and without rotation (e.g. see Koschmieder 1993; Bodenschatz *et al.* 2000), the radially travelling axisymmetric wave states have been quite elusive. Thompson *et al.* (2002) conducted a series of experiments on rotating convection in a cylinder of aspect ratio $\gamma = 11.8$ filled with water of Prandtl number $\sigma = 4.5$. They worked in a slow rotation regime ($\Omega \leqslant 28$) in order to keep the Froude number small ($F \leqslant 0.016$) as they wanted to keep the effects of centrifugal buoyancy small. For their slow rotations, the onset of convection is to a bulk Küppers–Lortz mode rather than the wall mode found at onset for faster rotations. By harmonically modulating the rotation of the cylinder, they were able to suppress the Küppers–Lortz mode and replace it by an axisymmetric target pattern. This target pattern, achieved by modulation of the rotation, was always observed to travel radially inward. They were unable to determine the cause of the inward drift of the patterns. They considered the large-scale circulation driven by the centrifugal buoyancy, but decided that this was an unlikely cause since their Froude number was so small. Theirs is the only experiment we are aware of in which sustained radially travelling target patterns have been observed in Rayleigh–Bénard convection.

Numerically, axisymmetric radially travelling target patterns have been found by Tuckerman & Barkley (1988), Siggers (2003) and in the present study. Tuckerman & Barkley (1988) considered non-rotating convection with $\gamma = 5$, $\sigma = 10$, with rigid no-slip boundaries and a non-insulating sidewall. Their non-rotating results are very similar to our $F = 0$ rotating results, with the conduction state losing stability to steady cellular ring states via a pitchfork bifurcation, and these undergoing a SNIC

bifurcation with another set of unstable cellular ring states which bifurcate from the unstable conduction state in a secondary pitchfork bifurcation as R is increased. Following the SNIC bifurcation, a limit-cycle state results which is very similar to the $F = 0$ travelling wave we report here. In particular, the pattern travels radially inward, as do ours and that found experimentally by Thompson *et al.* (2002).

On the other hand, the target patterns computed by Siggers (2003) travel radially outward. In those computations, the top and bottom boundaries were stress-free, there was no rotation, a small Prandtl number $\sigma = 0.1$ was used, and the aspect ratio was varied in the range $\gamma \in [4, 10]$. Not only did the direction of travel differ, but the onset was either via a Hopf bifurcation or a homoclinic saddle-loop bifurcation with reflection symmetry. This is in contrast to the SNIC bifurcation for onset of the travelling waves found by Tuckerman & Barkley (1988) and in this study.

Clearly, there is still much to learn about these travelling wave states. They are particularly interesting because they are patterns that travel in a direction which is neither periodic nor translation invariant. They have been computed to originate via a variety of bifurcations: SNIC bifurcations (Tuckerman & Barkley 1988, and us) and by Hopf and homoclinic/heteroclinic bifurcations (Siggers 2003), in rotating (Thompson *et al.* 2002, and us) and non-rotating systems (Tuckerman & Barkley 1988; Siggers 2003), and we have shown here that centrifugal buoyancy is not necessary for their onset or existence (our $F = 0$ results), but that even for moderately small $F > 0.17$, centrifugal buoyancy qualitatively changes the nature of the dynamics.

Our computational results presented here have imposed axisymmetry, and in the limit $F \to 0$ it is well known that in the R, Ω, γ, σ parameter regime studied the flows are unstable to three-dimensional instabilities and hence would not be observable in a physical experiment. However, it is still unknown whether for non-zero Froude number that is still the case. The large-scale circulation driven by the centrifugal force for non-zero Froude number has the potential to quench three-dimensional instabilities, in much the same way that the time-periodic large-scale circulation driven by the modulated rotation in the experiments of Thompson *et al.* (2002) quenches the three-dimensional flow, and so one may observe some of the axisymmetric dynamics reported here in parts of parameter space.

This work was supported by the National Science Foundation grant DMS-0509594, the Spanish Ministry of Science and Technology grant FIS2004-01336, and Spanish Ministry of Education and Science grant SAB2003-0172.

REFERENCES

Bajaj, K. M. S., Liu, J., Naberhuis, B. & Ahlers, G. 1998 Square patterns in Rayleigh-Bénard convection with rotation about a vertical axis. *Phys. Rev. Lett.* **81**, 806–809.

Barcilon, V. & Pedlosky, J. 1967 On the steady motions produced by a stable stratification in a rapidly rotating fluid. *J. Fluid Mech.* **29**, 673–690.

Benjamin, T. B. 1978*a* Bifurcation phenomena in steady flows of a viscous fluid. I. Theory. *Proc. R. Soc. Lond.* A **359**, 1–26.

Benjamin, T. B. 1978*b* Bifurcation phenomena in steady flows of a viscous fluid. II. Experiments. *Proc. R. Soc. Lond.* A **359**, 27–43.

Benjamin, T. B. & Mullin, T. 1981 Anomalous modes in the Taylor experiment. *Proc. R. Soc. Lond.* A **377**, 221–249.

Bodenschatz, E., Pesch, W. & Ahlers, G. 2000 Recent developments in Rayleigh-Bénard convection. *Annu. Rev. Fluid Mech.* **32**, 709–778.

Brummell, N., Hart, J. E. & Lopez, J. M. 2000 On the flow induced by centrifugal buoyancy in a differentially-heated rotating cylinder. *Theor. Comput. Fluid Dyn.* **14**, 39–54.

Buell, J. C. & Catton, I. 1983 Effect of rotation on the stability of a bounded cylindrical layer of fluid heated from below. *Phys. Fluids* **26**, 892–896.

Chandrasekhar, S. 1961 *Hydrodynamic and Hydromagnetic Stability*. Oxford University Press.

Daniels, P. G. 1980 The effect of centrifugal acceleration on axisymmetric convection in a shallow rotating cylinder or annulus. *J. Fluid Mech.* **99**, 65–84.

Goldstein, H. F., Knobloch, E., Mercader, I. & Net, M. 1993 Convection in a rotating cylinder. Part 1. Linear theory for moderate Prandtl numbers. *J. Fluid Mech.* **248**, 583–604.

Hart, J. E. 2000 On the influence of centrifugal buoyancy on rotating convection. *J. Fluid Mech.* **403**, 133–151.

Homsy, G. M. & Hudson, J. L. 1969 Centrifugally driven thermal convection in a rotating cylinder. *J. Fluid Mech.* **35**, 33–52.

Hu, Y., Ecke, R. & Ahlers, G. 1993 Convection near threshold for Prandtl numbers near 1. *Phys. Rev.* E **48**, 4399–4413.

Knobloch, E. 1998 Rotating convection: recent developments. *Intl J. Engng Sci.* **36**, 1421–1450.

Koschmieder, E. L. 1967 On convection on a uniformly heated rotating plane. *Beitr. Physik. Atmos.* **40**, 216–225.

Koschmieder, E. L. 1968 Convection on a non-uniformly heated, rotating plane. *J. Fluid Mech.* **33**, 515–527.

Koschmieder, E. L. 1993 *Bénard Cells and Taylor Vortices*. Cambridge University Press.

Küppers, G. & Lortz, D. 1969 Transition from laminar convection to thermal turbulence in a rotating fluid layer. *J. Fluid Mech.* **35**, 609–620.

Liu, Y. & Ecke, R. E. 2002 Nonlinear travelling waves in rotating Rayleigh-Bénard convection: Stability boundaries and phase diffusion. *Phys. Rev.* E **59**, 4091–4105.

Ning, L. & Ecke, R. E. 1993 Rotating Rayleigh-Bénard convection: Aspect-ratio dependence of the initial bifurcations. *Phys. Rev.* E **47**, 3326–3333.

Pfotenhauer, J. M., Niemela, J. J. & Donnelly, R. J. 1987 Stability and heat transfer of rotating cryogens. Part 3. Effects of finite cylindrical geometry and rotation on the onset of convection. *J. Fluid Mech.* **175**, 85–96.

Rossby, H. T. 1969 A study of Benard convection with and without rotation. *J. Fluid Mech.* **36**, 309–335.

Royer, J. R., O'Neill, P., Becker, N. & Ahlers, G. 2004 Wave-number selection by target patterns and sidewalls in Rayleigh-Bénard convection. *Phys. Rev.* E **70**, 036313.

Rüdiger, S. & Knobloch, E. 2003 Mode interaction in rotating Rayleigh-Bénard convection. *Fluid Dyn. Res.* **33**, 477–492.

Sánchez-Álvarez, J. J., Serre, E., Crespo del Arco, E. & Busse, F. H. 2005 Square patterns in rotating Rayleigh-Bénard convection. *Phys. Rev.* E **72**, 036307.

Siggers, J. H. 2003 Dynamics of target patterns in low-Prandtl-number convection. *J. Fluid Mech.* **475**, 357–375.

Thompson, K. L., Bajaj, K. M. S. & Ahlers, G. 2002 Travelling concentric-roll patterns in Rayleigh-Bénard convection with modulated rotation. *Phys. Rev.* E **65**, 04618.

Tuckerman, L. S. & Barkley, D. 1988 Global bifurcation to travelling waves in axisymmetric convection. *Phys. Rev. Lett.* **61**, 408–411.

Veronis, G. 1959 Cellular convection with finite amplitude in a rotating fluid. *J. Fluid Mech.* **5**, 401–435.

Zhong, F., Ecke, R. & Steinberg, V. 1991 Asymmetric modes and the transition to vortex structures in rotating Rayleigh-Bénard convection. *Phys. Rev. Lett.* **67**, 2473–2476.

Zhong, F., Ecke, R. & Steinberg, V. 1993 Rotating Rayleigh-Bénard convection: asymmetric modes and vortex states. *J. Fluid Mech.* **249**, 135–159.